Surface Forces and Drag Coefficients of Microspheres near a Plane Surface Measured with Optical Tweezers

Erik Schäffer*

Max Planck Institute of Molecular Cell Biology and Genetics, Pfotenhauerstrasse 108, 01307 Dresden, Germany

Simon F. Nørrelykke

Max Planck Institute for the Physics of Complex Systems, Nöthnitzer Strasse 38, 01187 Dresden, Germany

Jonathon Howard

Max Planck Institute of Molecular Cell Biology and Genetics, Pfotenhauerstrasse 108, 01307 Dresden, Germany

Received July 28, 2006. In Final Form: January 11, 2007

Optical tweezers are widely used to measure molecular forces in biology. Such measurements are often influenced by a nearby surface that can perturb both the calibration of the tweezers as well as the hydrodynamic forces acting on microspheres to which the biomolecules are attached. In this study, we have used a very stable optical tweezers setup employing a recently developed calibration method (Tolić-Nørrelykke, S. F.; Schäffer, E.; Howard, J.; Pavone, F. S.; Jülicher, F.; Flyvbjerg, H. *Rev. Sci. Instrum.* **2006**, *77* (10), 103101) to determine how the calibration of the tweezers and the forces on the microspheres depend on the height above the surface. We show that the displacement sensitivity of the tweezers is modulated by a standing light wave between the microsphere and the surface. We measured the dependence of the drag coefficient on height and compared it to exact and closed-form solutions to the Navier−Stokes equations. Also, we measured the surface force gradients in different salt solutions and for different surface blocking methods. For a given blocking method, our data suggest that microspheres can experience attractive and/or repulsive forces close to surfaces. For example, a Teflon layer reduces attractive interactions, and the presence of casein can lead to long-range repulsive interactions. These measurements are a prerequisite for the accurate measurement of normal forces with respect to an interface that occur in biological molecules held between surfaces.

1. Introduction

In biophysical experiments employing optical tweezers, spherical beads are often used as handles to study the mechanical properties of biomolecules such as motor proteins and DNA.[2,3] However, such experiments are in many cases performed near a plane surface, namely, a glass coverslip, and the static and dynamic forces between the beads and the surface can profoundly influence the outcomes of these experiments. For example, close-range adhesive forces between the beads and the surface can lead to immobilization of the beads on the surface. This means that the surfaces usually have to be pacified by other proteins or surfactants. Another example is the well-known "wall effect"[4] that nearby surfaces have on the hydrodynamical properties of colloids; this leads to problems when estimating the drag forces on the beads which in turn can lead to problems calibrating the optical forces. Other problems include long-range repulsive surface forces that might mask the biological forces, aberrations, and optical reflections between the bead and the surface that can lead to uncertainties in calibration.[3] Thus accurate measurement of forces in biological molecules using optical tweezers requires precise understanding of these surface forces. The goal for the present work is to measure these forces.

Several techniques have been used to study surface forces. The surface force apparatus[5] and the atomic force microscope[6] have been used to test the Derjaguin−Landau−Verwey−Overbeek (DLVO) theory for the static forces between surfaces. Because these techniques have limited force resolution, total internal reflection microscopy[7] and optical tweezers[8,9] have been used to extend the force sensitivity for micron sized colloids down to the pN range.

In the present study, we have used an optical tweezers setup with axial position detection based on back-focal-plane interferometry[10] combined with a novel calibration method.[1] This setup has a significantly better spatial resolution than earlier tweezers measurements ($\lesssim$1 nm with a 10 kHz bandwidth) and does not require assumptions about the bead radius or solution viscosity. We were able to accurately determine the surface position to within a few nanometers. Our ability to calibrate the optical tweezers very precisely in the axial direction allowed us to estimate with very high resolution the magnitude of the surface

* Corresponding author. Current address: Center of Biotechnology, Technical University Dresden, Tatzberg 47−51, 01307 Dresden, Germany.

(1) Tolić-Nørrelykke, S. F.; Schäffer, E.; Howard, J.; Pavone, F. S.; Jülicher, F.; Flyvbjerg, H. *Rev. Sci. Instrum.* **2006**, *77* (10), 103101.
(2) Howard, J. *Motor Proteins and the Cytoskeleton*; Sinauer Associates: Sunderland, MA, 2001.
(3) Neuman, K.; Block, S. *Rev. Sci. Instrum.* **2004**, *75* (9), 2787−2809.
(4) Happel, J.; Brenner, H. *Low Reynolds Number Hydrodynamics*; Martinus Nijhoff Publishers: The Hague, 1983.
(5) Israelachvili, J. N. *Intermolecular and Surface Forces*; Academic Press: London, 1991.
(6) Ducker, W. A.; Senden, T. J.; Pashley, R. M. *Langmuir* **1992**, *8* (7), 1831−1836.
(7) Prieve, D. C. *Adv. Colloid Interface Sci.* **1999**, *82* (1−3), 93−125.
(8) Clapp, A. R.; Dickinson, R. B. *Langmuir* **2001**, *17* (7), 2182−2191.
(9) Hansen, P. M.; Dreyer, J. K.; Ferkinghoff-Borg, J.; Oddershede, L. *J. Colloid Interface Sci.* **2005**, *287* (2), 561−571.
(10) Pralle, A.; Prummer, M.; Florin, E. L.; Stelzer, E. H. K.; Hörber, J. K. H. *Microsc. Res. Tech.* **1999**, *44* (5), 378−386.

10.1021/la0622368 CCC: $37.00
Published on Web 02/28/2007

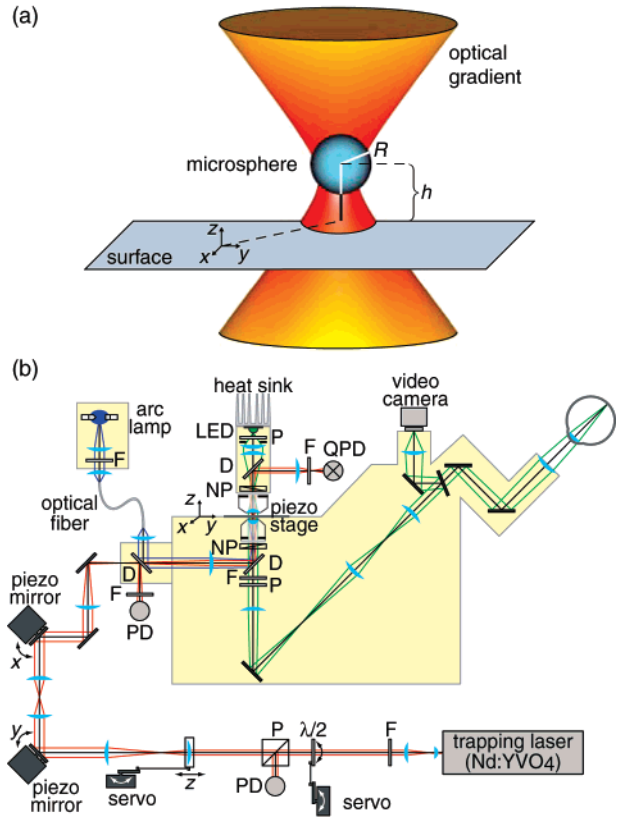

Figure 1. (a) Setup geometry: A microsphere (bead) with radius R is trapped in a tightly focused laser beam near a surface. The bead center−surface separation is denoted by h and the axial direction (along the axis of the laser) is referred to as z. The origin of the coordinate system is the projection of the trap center onto the surface. It is displaced for clarity. (b) Schematic drawing of the optical tweezers apparatus. D, dichroic mirror; F, filter; $\lambda/2$, half-wave plate; LED, light emitting diode; NP, Nomarski prism; (Q)PD, (quadrant) photodiode; P, polarizer.

forces between the cover glass and the bead based on the measured axial trap stiffness. Using this method, we studied the interaction of silica and polystyrene microspheres with glass and modified glass surfaces in solutions of various ionic strengths. For instance, a thin Teflon film index-matches water and thereby screens the attractive van der Waals interactions. Of particular biophysical interest, we determined how the protein casein, which is often used in assays on motor proteins, can influence the surface interactions. Because the calibration method employed here[1] does not assume that the value of the drag coefficient is known, it can be used to measure how a nearby surface influences the hydrodynamic forces on a bead. We tested and found very good agreement with Faxén's law[4] for the lateral drag and closed-form interpolation formulas that approximate an exact solution to the Navier−Stokes equations[11] for the axial drag perpendicular to the surface.

2. Materials and Methods

2.1. Optical Tweezers Setup. The microsphere is held in an optical trap (Figure 1a) built around an inverted microscope (Zeiss Axiovert 135 TV) on an optical table (Figure 1b). The laser is a diode-pumped neodymium vanadate crystal (Nd:YVO_4) with 1.5 W at $\lambda_0 = 1064$ nm and an M^2 value of ∼1.25 (Smart Laser Systems, Berlin, Germany). It is linearly polarized normal to the optical table. In the imaging plane, the polarization is in the y direction (Figure 1a). To increase the mechanical stability, the laser beam is kept 50 mm off the optical table. The laser is expanded to a final beam diameter of ∼6 mm. With a half-wave plate placed before the polarizer, the laser intensity can be varied by rotating the plate with a toy model servo. The lenses, antireflection coated achromats (LINOS Photonics, Göttingen, Germany), have the following focal lengths in millimeters (starting from the laser): 6, 40, 80, 120, 140, 140, 160, and 160. All optics are mounted on four rods (Microbench system, LINOS Photonics) clamped to the optical table and enclosed in an anodized aluminum box. The piezo-steering mirrors (S-226.00, Physik Instrumente (PI), Karlsruhe, Germany) are placed in conjugate planes of the back aperture of the objective such that the beam pivots around this point with a constant transmitted laser intensity.[12] In this way, the trap stiffness does not change while steering.

The main difference between our setup and most others is the control of the laser focus height relative to the imaging plane. To this end, we move the first lens after the polarizer with a servo. The position and focal length of the lens are chosen such that no changes in the intensity occur upon moving the lens.[12] In the imaging plane, the laser focus moves less than 20 nm laterally per 1 μm of axial motion. One advantage of this method is that imaging is not impaired by the movement of the laser. The lens movement is calibrated by comparing the change in the laser waist in the back focal plane of the condenser upon moving either the lens or the imaging objective by a known distance. A translation of the lens by 1 mm is equivalent to a 195 ± 4 nm height change of the imaging objective or alternatively the axial stage position. The value is in reasonable agreement with the expected value of 182 nm based on the focal lengths of all lenses along the optical path.[12]

The remaining apparatus is composed of a three-axis piezoelectric translation stage (*xyz*: P-733.3DD, PI) that has been embedded in a solid block of aluminum mounted directly on the table and the microscope. The objective is clamped to this block to prevent drift and mechanical vibrations. We used a Zeiss Plan-Neofluar 100×, 1.3 NA, oil-immersion objective with a back aperture of 6 mm. The samples are mounted on a small $x-y$ translation stage (07 TMC 511, Melles Griot) with 6 mm travel distance which is fixed on the piezo stage. The custom-built condenser, which uses a Zeiss Plan-Neofluar 40×, 1.3 NA, oil-immersion objective, sits on three fine-adjustment screws on top of the same block and uses a light emitting diode (LED)—a green Luxeon V star emitter (LXHL-LM5C, Lumileds Lighting, San Jose, USA) with 5 W power.[13] A dichroic mirror inside the condenser reflects the laser light onto a photodiode for back-focal-plane detection in three dimensions.[10,14] Position detection is obtained with either a quadrant photodiode, QP50-6SD, or a position sensing photodiode, DL100-7PCBA (both Pacific Silicon Sensors Inc., USA). The diodes are mounted on a small $x-y$ translation stage. The z signal is based on variations of the total laser intensity measured in the back focal plane of the condenser.[10] For small displacements, the laser intensity is a monotonic function of axial particle position, linear within 5% for about ±250 nm relative to the laser focus. The modulation corresponding to the axial signal is typically only a few percent of the total laser intensity signal. The laser intensity was stable enough that normalization of the x, y, and z signals by the intensity measured in the back focal plane or the epifluorescence port was not necessary.[3]

Using the LED produced much less heat than a conventional light source and therefore reduced thermal drift. The LED condenser permits video-enhanced differential interference contrast with a standard video camera (LCL-902HS, Watec, Japan) and can resolve single microtubules and surface features of ≲1 nm in thickness.[13] The video-enhanced differential interference contrast microscopy was used to monitor the cleanness and flatness of the substrates while the measurements were performed. Fluorescence imaging is possible as well. Three temperature sensors are mounted on the setup: one attached to each objective and one to the aluminum block in which the piezo stage is embedded. The temperature is recorded every second with a resolution of <0.1 °C (type-T

(11) Brenner, H. *Chem. Eng. Sci.* **1961**, *16*, 242−251.

(12) Fällman, E.; Axner, O. *Appl. Opt.* **1997**, *36* (10), 2107−2113.
(13) Bormuth, V.; Howard, J.; Schäffer, E. *J. Microsc.* **2007**, *225*, 1−5.
(14) Gittes, F.; Schmidt, C. F. *Biophys. J.* **1998**, *74* (2), A183−A183.

thermocouples, IT-23 Physitemp, Clifton, USA). The whole setup is controlled via custom-written software using LabView (National Instruments, USA).

One important requirement to obtain high-resolution data is the stability of the trapping laser with regard to intensity and pointing angle. We modified the laser such that the pumping laser is passively cooled and mounted on the optical table. This improved the pointing stability considerably (data not shown). Furthermore, the intensity is stabilized by a feedback: the laser intensity is measured by a photodiode at the epifluorescence port of the microscope, and this signal is used to modulate the pumping laser current to keep the laser intensity constant. With the feedback on, the laser intensity has a 0.01% coefficient of variation (standard deviation divided by the mean) measured over a period of 200 s. The laser angle has a standard deviation of 0.2 μrad in the x direction and 0.06 μrad in the y direction. With a conversion factor of 0.23 nm per μrad, the pointing stability results in less than 0.3 nm peak-to-peak movement in the image plane.

The overall system noise of the tweezers setup was measured using a probe tightly coupled to the surface. Data sampled over 1 s with a bandwidth of 50 kHz show a standard deviation of the position signals of <0.5 nm in all three directions. Figure 2a shows the capabilities of the instrument: 5 Å steps were easily resolved when the laser was scanned past an immobilized bead in a stepwise manner using the piezo mirrors while recording the signal by the detection system. Here, a 528 nm diameter PS bead was passively adsorbed onto a cleaned glass coverslip in a 0.1 M KCl solution. The peak-to-peak noise is less than 1 nm with a bandwidth of 10 kHz (gray line). Adjacent averaging of 1000 data points (orange line) clearly demonstrates sub-nanometer resolution.

2.2. Microspheres and Flow Cell Preparation. Polystyrene (PS) microspheres from Polysciences (Warrington, USA) were 528 nm in diameter with a 2% coefficient of variation. Transmission electron microscopy that we performed indicated a 1.2% coefficient of variation for these microspheres. Silica beads from Bangs Laboratories (Fishers, USA) were 0.60 μm in diameter with a coefficient of variation of 10%. The nonfunctionalized beads were washed in demineralized and purified water (grade 1 with a conductivity of 0.055 μS/cm), centrifuged, and sonicated for resuspension twice.

Flow cells with a 3 mm wide channel consisted of one 18 mm^2 coverslip No. 1.5 (Corning, USA) on top of a 22 mm^2 coverslip. Before use, the coverslips were washed and sonicated in separate baths of detergent, ethanol, and purified water. Blocked surfaces were prepared by two methods. Coverslips were rendered hydrophobic by either using dichlorodimethylsilane (DDMS) following standard procedures[15] or by spin-coating at 2000 rpm in a nitrogen atmosphere a thin polymer layer (<100 nm thick) using a 0.5% solution of Teflon AF 1600 (DuPont) dissolved in the perfluoro compound FC-75 (Acros Organics). The resulting Teflon film has a refractive index of 1.31 and thus almost index-matches water. Therefore, the attractive van der Waals interaction between a bead and a Teflon-coated surface is reduced.[5] In the flow cell, the coverslips were separated by a layer of Parafilm. The Parafilm was melted by placing the sample on a 100 °C hot plate. Cooling then glued the coverslips together. After assembly of the flow cell, a 1% aqueous solution of Pluronic F127 (referred to as F127 below) (Sigma) was flowed in, incubated for 15 min, and the flow cell rinsed thoroughly afterward. Finally, the solution of interest containing the microspheres was flowed in, and the ends of the chamber were sealed with vacuum grease to avoid sample evaporation. We did not use double sticking tape and nail polish for sealing because these materials were observed to contaminate the solutions. This contamination showed up as a decrease in the measured screening length (see eq 2 and section 3.2.2).

F127 is a triblock copolymer consisting of two outer poly(ethylene oxide) (PEO) and an inner poly(propylene oxide) (PPO) block with 100 and 65 monomers, respectively. The molecular weight is 12.6 kDa. The PPO block is hydrophobic and strongly adsorbs onto the hydrophobic DDMS or Teflon layer. The outer PEO parts form a polymer brush (PEO is also known as PEG) that has been shown to be very effective in blocking protein adsorption in single molecule experiments.[15] Surfaces treated in this manner are also very effective in preventing microspheres from adsorbing to the surface. With the brush density[16] of $\rho = 0.23$ (PEO chains)/nm^2 and a monomer size $a = 0.35$ nm, the brush thickness is $L = aN(a^2\rho)^{1/3} \approx 10$ nm, where N is the number of monomers in the PEO blocks.[17]

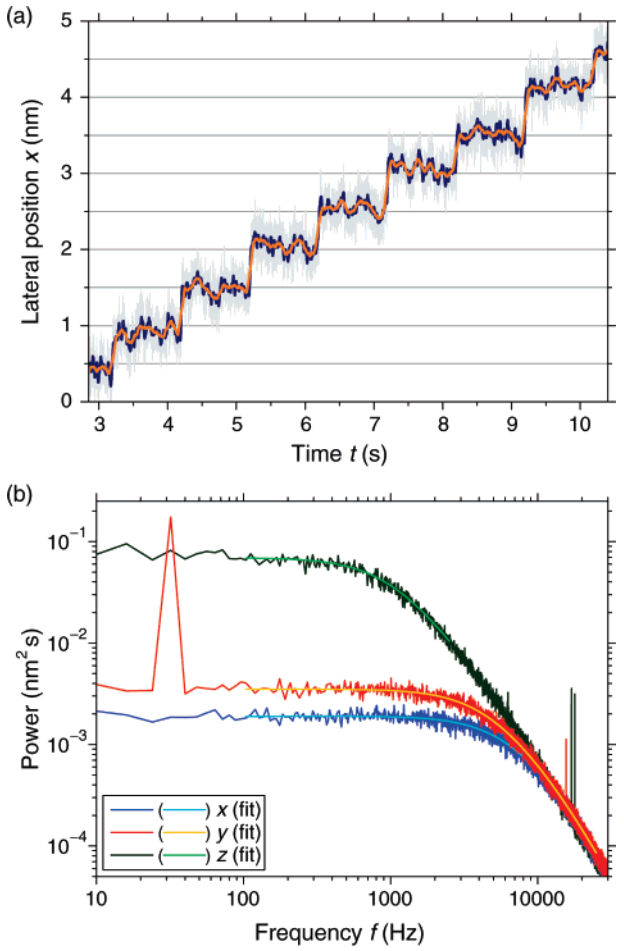

Figure 2. (a) Time trace of the trapping laser scanned with the piezo mirrors in 5 Å steps past a fixed PS bead of diameter 528 nm in the x direction. The gray line shows the raw data sampled with 10 kHz. Adjacent averaging of 200 (1000) data points, blue (orange) line, demonstrates subnanometer resolution with a standard deviation of ~0.06 nm over 1 s (a step plateau). (b) Calibrated power spectral density for all directions with $(\kappa_x, \kappa_y, \kappa_z) = (0.203 \pm 0.002, 0.147 \pm 0.001, 0.0322 \pm 0.0003)$ pN/nm of a 600 nm diameter silica bead with a bead−surface separation of 2040 nm. Differences between the lateral directions (x and y) arise from the polarization of the laser in the y direction. The calibration spike in the y direction at $f_{stage} = 32$ Hz corresponds to a bead motion of 1.67 nm amplitude. The stage was driven with $A = 250$ nm. The power spectra are the average of 100 independent power spectra each. The sampling frequency was 65 536 Hz, the measurement time for each spectrum was $t_{msr} = 0.125$ s, and the temperature was 26.6 °C. The noise peaks at $f > 5$ kHz are excluded from the fits.

2.3. Data Acquisition and Fitting. Signals were recorded with a 24-bit data acquisition card (NI 4472, National Instruments) which has a 45 kHz alias-free bandwidth. Data were read out with a rate of 65 536 samples per second unless otherwise noted. For the calculation of one power spectrum, we used 8192 data points. One hundred consecutive power spectra were averaged and automatically fitted with a custom-written least-squares fitting routine implementing

(15) Helenius, J.; Brouhard, G.; Kalaidzidis, Y.; Diez, S.; Howard, J. *Nature* **2006**, *441* (7089), 115−119.

(16) Li, J. T.; Caldwell, K. D. *Langmuir* **1991**, *7* (10), 2034−2039.

(17) Halperin, A. *Langmuir* **1999**, *15* (7), 2525−2533.

a Levenberg−Marquardt algorithm. Each datum was weighted by its theoretical error bar.[18] Data points which deviated more than five standard deviations from the fit were automatically excluded. This applied to the calibration peak and electronic noise.

To fit the power spectra, we used either a Lorentzian (see section 2.4 and Tolić-Nørrelykke et al.[1]) or eq 32 from Berg-Sørensen et al.[18] Because silicon photodiodes act as low-pass filters at a wavelength of 1064 nm,[18−20] we used eq 35 from Berg-Sørensen et al.[18] to account for this parasitic filtering. Equation 32 from Berg-Sørensen et al.[18] accounts for the frequency-dependent hydrodynamics far away from surfaces (in bulk). Close to a surface, using either eq 32 from Berg-Sørensen et al.[18] or a Lorentzian, is an approximation that worked well in combination with the parasitic filter within the accuracy considered in this study. Qualitatively, the deviation from a Lorentzian due to the frequency dependence of the drag is reduced upon approaching a surface. The overall shape of the power spectrum to a first-order approximation resembles a low-pass filtered Lorentzian. Thus, the frequency dependence can largely be absorbed into the parameters that describe the parasitic filter. Equations[1] that approximate the frequency dependence near a wall to within 1% are only valid down to distances of $h/R = 1.5$. The distances in this study reach smaller values than this. Thus, there is no accurate theoretical description for all of our data at present. We therefore used the phenomenological approximation of eq 32 from Berg-Sørensen et al.[18] or a Lorentzian in combination with a low-pass filter. The error that arises due to neglecting the frequency dependence of the drag is $\lesssim$1% for our beads and experimental conditions (for a detailed discussion, see Tolić-Nørrelykke et al.[1]). Inertial effects are even smaller.[1] Because these errors are smaller than the relative error, for example, of the calibration (∼2%) at a single height or of the Debye length (∼15% mainly caused by thermal drift), we neglect their effect.

2.4. Theoretical Background. *2.4.1. Surface Forces*. Using the DLVO theory, the interaction energy between a sphere and a flat surface with a separation of $h - R$ can be approximated by[5,21]

$$\phi(h) = \phi_0 e^{-(h-R)/L} - \frac{H}{6}\left[\frac{R}{h-R} + \frac{R}{h+R} + \ln\left(\frac{h-R}{h+R}\right)\right] \quad (1)$$

The first term on the right-hand side models the electrostatic interactions characterized by the Debye screening length

$$L = \sqrt{\frac{\epsilon_w \epsilon_0 k_B T}{e^2 \sum_i \rho_i \zeta_i^2}} \cong \frac{0.304}{\sqrt{[\mathrm{KCl}]}}\mathrm{nm} \quad (2)$$

with the permittivity of water and vacuum, ϵ_w and ϵ_0, respectively, the Boltzmann constant k_B, the temperature T, the elementary charge e, and the density of the ith ion ρ_i and corresponding valency ζ_i. The electrolyte concentration [KCl] is in moles per liter. The amplitude is $\phi_0 = 4\pi\epsilon_w\epsilon_0\psi_0^2 R$ where ψ_0 is the effective surface potential. The second term in eq 1 describes the van der Waals interactions, the magnitude of which are characterized by the Hamaker constant H which depends on the dielectric properties of the media.

2.4.2. Trapped Sphere near a Surface: Equation of Motion. Ignoring frequency dependence and inertial effects (as justified above and in Tolić-Nørrelykke et al.[1]), the equation of motion at time t for a microsphere with position $\boldsymbol{r} = (x, y, z)$ trapped in an optical potential close to a surface (Figure 1a) is given by

$$\Gamma\frac{d}{dt}[\boldsymbol{r} - \boldsymbol{r}_{\mathrm{stage}}] + \nabla E = \boldsymbol{F}_T(t) \quad (3)$$

with the drag coefficient matrix Γ. Here, the sample stage drives the flow cell sinusoidally with amplitude A and frequency f_{stage} relative to the optical trap, $\boldsymbol{r}_{\mathrm{stage}} = A\sin(2\pi f_{\mathrm{stage}} t)\hat{\boldsymbol{y}}$, where $\hat{\boldsymbol{y}}$ is the unit vector in the y direction. The first term on the left-hand side of eq 3 is the drag force proportional to the bead velocity relative to the stage. The second term describes the surface and trapping force. It is the gradient of the potential energy

$$E = \frac{1}{2}(\kappa_x x^2 + \kappa_y y^2 + \kappa_z (z - h_0)^2) + \phi(z) \quad (4)$$

where κ_i denotes the trap stiffness in the i direction with $i = x, y, z$ and h_0 is the axial center position of the optical trapping potential. The right-hand side of eq 3 is a random thermal force driving the Brownian motion.[1] The diagonal elements of the drag coefficient matrix are $\Gamma_{ii} = \{\gamma_{xx}, \gamma_{yy}, \gamma_{zz}\}$, and the off-diagonal elements are zero. We denote the lateral drag coefficient as $\gamma_{\parallel} \equiv \gamma_{xx} = \gamma_{yy}$ and the axial one as $\gamma_{\perp} \equiv \gamma_{zz}$. Both depend on the distance of the bead center to the surface, h. The height dependence is approximated by Faxén's law[4]

$$\gamma_{\parallel} = \frac{\gamma_0}{1 - \frac{9R}{16h} + \frac{R^3}{8h^3} - \frac{45R^4}{256h^4} - \frac{R^5}{16h^5}} \quad (5)$$

for the lateral directions and by Brenner's infinite sum formula[11] for the axial direction. Because the latter formula is inconvenient and converges slowly for small separations, we developed interpolation formulas that deviate less than 1% from the exact formula over the complete range of possible separations. We give the equations and their derivations in Appendix A. Here, we use a 12th-order interpolation formula with six coefficients for the axial drag

$$\gamma_{\perp} = \frac{\gamma_0}{1 - \frac{9R}{8h} + \frac{R^3}{2h^3} - \frac{57R^4}{100h^4} + \frac{R^5}{5h^5} + \frac{7R^{11}}{200h^{11}} - \frac{R^{12}}{25h^{12}}} \quad (6)$$

which deviates less than 0.1% from Brenner's exact formula for $h/R \gtrsim 1.1$ and less than 0.3% over the whole range of h. The interpolation is exact in both limits of h going to R and ∞. For $h \to \infty$, in the zero-frequency limit considered here, $\gamma_{\parallel} = \gamma_{\perp} = \gamma_0 \equiv 6\pi\eta R$, which is the bulk drag coefficient corresponding to Stokes drag with viscosity η.

2.4.3. Calibration. The calibration is based on a power spectral analysis. Solving eq 3 in Fourier space results in a power spectral density (PSD) which is a Lorentzian for all spatial directions with a delta function spike at f_{stage} in the direction in which the stage is driven.[1] The Lorentzian is characteristic for the Brownian motion of a trapped object in a parabolic potential. Examples of power spectra are shown in Figure 2b. Note that the spike consists of a single datum since the driving frequency is an integer multiple of the power spectrum's frequency resolution.[1] It appears wide because of the chosen frequency resolution (8 Hz in Figure 2b). Every axis has a characteristic corner frequency $f_c = \kappa/(2\pi\gamma)$ and a plateau value *proportional* to the diffusion coefficient $D = k_B T/\gamma$. Because the drag coefficient γ depends on h, both f_c and D depend on the distance to the surface.

Three parameters need to be determined by the calibration: the displacement sensitivity, the drag coefficient, and the trap stiffness. An experimental power spectrum obtained with a photodiode is measured in (volts)^2 × (seconds) with the scale set by the volt-to-meter displacement sensitivity β. The integrated power in the spike, W_{ex}, is therefore measured in (volts)^2. On the other hand, since it is the response of a driven harmonic oscillator, the power is known a priori in (meters)^2 and thus serves as a "scale bar". Hence, the displacement sensitivity for the driven axis is given by[1]

$$\beta = \sqrt{\frac{W_{\mathrm{th}}}{W_{\mathrm{ex}}}} = A(2P_{\mathrm{spike}}\Delta f\,[1 + (f_c/f_{\mathrm{stage}})^2])^{-1/2} \quad (7)$$

(18) Berg-Sørensen, K.; Flyvbjerg, H. *Rev. Sci. Instrum.* **2004**, *75* (3), 594−612.
(19) Berg-Sørensen, K.; Oddershede, L.; Florin, E. L.; Flyvbjerg, H. *J. Appl. Phys.* **2003**, *93* (6), 3167−3176.
(20) Berg-Sørensen, K.; Peterman, E. J. G.; Weber, T.; Schmidt, C. F.; Flyvbjerg, H. *Rev. Sci. Instrum.* **2006**, *77* (6), 063106.
(21) Hamaker, H. C. *Physica* **1937**, *4*, 1058−1072.

with units (meters)/(volt). Here, W_{th} and W_{ex} denote the theoretically expected and experimentally determined power in the spike, respectively, and P_{spike} is the PSD at the stage frequency—the height of the spike—with the Brownian motion subtracted measured in $(volts)^2 \times (seconds)$. The frequency resolution of the power spectra is given by $\Delta f = 1/t_{msr}$ where t_{msr} is the measurement time. The drag coefficient for the driven axis is

$$\gamma = \frac{k_B T}{\beta^2 D_{volts}} \tag{8}$$

and the trap stiffness is

$$\kappa = 2\pi f_c \gamma \tag{9}$$

where the corner frequency, f_c, and the diffusion coefficient, D_{volts}, with units $(volts)^2/(seconds)$ are obtained from a fit to the power spectrum (see section 2.3). All the other parameters in the above equations are known. Thus, within the approximation of a frequency-independent drag, the system can be calibrated in the driven direction without any assumptions. We elaborate below (see section 3.1) how driving one axis can be sufficient for the calibration of all spatial dimensions.

2.4.4. Surface Force Probing. The surface forces influence the trapping conditions. However, only the axial direction is affected by the surface potential. The surface force produces two effects. First, the mean axial trapping position is shifted so that the optical forces balance the surface force, and second, the axial trap stiffness is changed. A Taylor expansion of the surface interaction energy ϕ around the mean position h of the center of the bead together with eq 3 yields[8]

$$h = h_0 - \frac{\phi'(h)}{\kappa_z} = h_0 + \Delta h \tag{10}$$

$$\kappa_z^{eff} = \kappa_z + \phi''(h) \tag{11}$$

where a prime denotes a derivative with respect to z, and Δh is the axial distance that the bead is displaced from the trap center. For example, for a repulsive surface interaction, the bead is pushed away from the surface ($\phi' < 0$ and $\Delta h > 0$, eq 10), and the effective axial trap stiffness κ_z^{eff} is increased ($\phi'' > 0$, eq 11). An attractive interaction has the opposite effect.

The equations above motivate how surface forces can be measured. Equation 10 indicates that the surface force ($-\phi'$) can be obtained by measuring $\kappa_z \Delta h$. This effect of the surface force on the mean bead position has been utilized in earlier studies.[8,9] Equation 11 shows that the surface force gradient (ϕ'') is given by the deviation of the axial trap stiffness from its value far away from the surface κ_z. In this work, we take advantage of our calibration procedure in order to measure the effective axial trap stiffness κ_z^{eff} and in this way determine the surface force gradients.

2.5. Focal Shift. Aberrations caused by the refractive index mismatch of glass and water influence the trapping position relative to the surface. We controlled the relative distance of the bead to the surface by either changing the position of the movable lens or by displacing the piezo stage. Both methods yielded equivalent results. We denote the relative position—controlled either by the lens or the stage (see section 2.1)—by h_{stage}. The bead center−surface distance without surface effects ($\phi = 0$) is then given by

$$h_0 \equiv h|_{\phi=0} = (h_{stage} - h_{surf})\delta \tag{12}$$

where δ denotes the focal shift and h_{surf} is the surface position. For $h = h_0$, the mean trapping position co-moves with the laser focus and by a relative amount with the stage. The focal shift is $\delta_w \approx 1$ for a water immersion objective with properly adjusted correction collar and $\delta_{oil} \approx 0.81$ for an oil immersion objective with spherical aberrations when used to image in an aqueous medium.[3,22] We used an oil-immersion objective and kept the value of the focal shift fixed at 0.81. This is the average value that we have independently confirmed by three methods: first, by measuring the intensity variation as a function of distance,[22] second, by using δ as a fit parameter in eqs 5 and 6, and third, by looking at the periodic modulation of the displacement sensitivity (see below). We observed that the value of δ varied by a few percent for individual beads.

2.6. Lateral Calibration. In order to perform quantitative axial measurements, we first calibrated one lateral direction as a function of distance from the surface to determine the surface position, h_{surf}, and the Stokes' bulk drag coefficient, γ_0. A trapped bead was calibrated at several distances from the surface by driving the stage in one lateral dimension only—we chose the *y*-axis because the pointing stability of the laser was best in this direction (Figure 3). The power spectra for the other dimensions were recorded simultaneously (see Figure 2b). For the data in this section, we chose a high ionic strength and a blocked surface to minimize surface interactions, thus we set $\phi = 0$ in the data analysis. We used a 528 nm diameter PS bead in a 0.1 M KCl solution with a F127-blocked surface. The stage was driven with $A = 150$ nm and $f_{stage} = 32$ Hz. At each of ~50 positions, 100 power spectra were acquired, averaged, and analyzed automatically as described in section 2.3. The laser height was controlled with the movable lens. The equivalent stage movement is quoted on the bottom axis. The upper axis shows the corresponding bead center position h_0 according to eq 12. The vertical gray line indicates the sphere's radius R. At this position, the bead touches the surface. Figure 3a−c shows the displacement sensitivity β, the drag coefficient γ, and the trap stiffness κ for each height resulting from eqs 7−9, respectively.

The displacement sensitivity β is not a constant as sometimes assumed.[9] As a function of stage height, there is a small overall increase with increasing h expected from aberrations.[23] Furthermore, β shows a clear sinusoidal modulation with a periodicity of 488 ± 14 nm and an amplitude of ~2.2% relative to the mean value (Figure 3a). The modulation is caused by light scattered back from the microsphere. This light, upon reflecting from the surface, interferes with the incoming laser light and forms a standing light wave. The periodicity of this interference pattern is expected to be $\lambda_0/(2n_w) = 400$ nm where $n_w = 1.33$ is the refractive index of water. Thus, the ratio of the observed to the expected periodicity can be used to determine the focal shift which resulted in $\delta = 0.82 \pm 0.02$. This value is expected[3,22] and constitutes a self-consistency check for the system. If β is assumed to be constant in a power spectral analysis, for example, based on a fixed-bead calibration,[3] the modulation in β is falsely reflected in a modulation of the values of the drag coefficient.[24]

The dependence on height of the drag coefficient $\gamma_{||}$ for our data is consistent with the hydrodynamic theory. In Figure 3b, the measured drag coefficients are plotted as a function of h. They are normalized by the value of the expected Stokes drag γ_0^{spec} far from the surface based on the specifications of the bead radius and a temperature measurement. The measured value γ_0 can differ from γ_0^{spec} if, for instance, the bead radius deviates from the specifications; γ_0 is obtained from a fit of Faxén's law (eq 5) using eq 12 (solid line in Figure 3b). For the *chosen* bead yielding the results in Figure 3, there is excellent agreement with the expected value: $\gamma_0/\gamma_0^{spec} = 1.004 \pm 0.004$ (see also Appendix B and Tolić-Nørrelykke et al.[1]). The other fit parameter is $h_{surf} = -0.347 \pm 0.002$ μm. The surface position is thus determined within 2 nm. Upon approaching the surface, the lateral drag coefficient increases by more than a factor of 2 compared to the Stokes drag. Faxén's law, however, is only a good approximation up to $\gamma_{||}/\gamma_0 \lesssim 1.7$.[25] We

(22) Neuman, K. C.; Abbondanzieri, E. A.; Block, S. M. *Opt. Lett.* **2005**, *30* (11), 1318−1320.
(23) Vermeulen, K. C.; van Mameren, J.; Stienen, G. J. M.; Peterman, E. J. G.; Wuite, G. J. L.; Schmidt, C. F. *Rev. Sci. Instrum.* **2006**, *77* (1), 013704.
(24) Pralle, A.; Florin, E. L.; Stelzer, E. H. K.; Hörber, J. K. H. *Appl. Phys. A: Mater. Sci. Process.* **1998**, *66*, S71−S73.
(25) Goldman, A. J.; Cox, R. G.; Brenner, H. *Chem. Eng. Sci.* **1967**, *22* (4), 637−651.

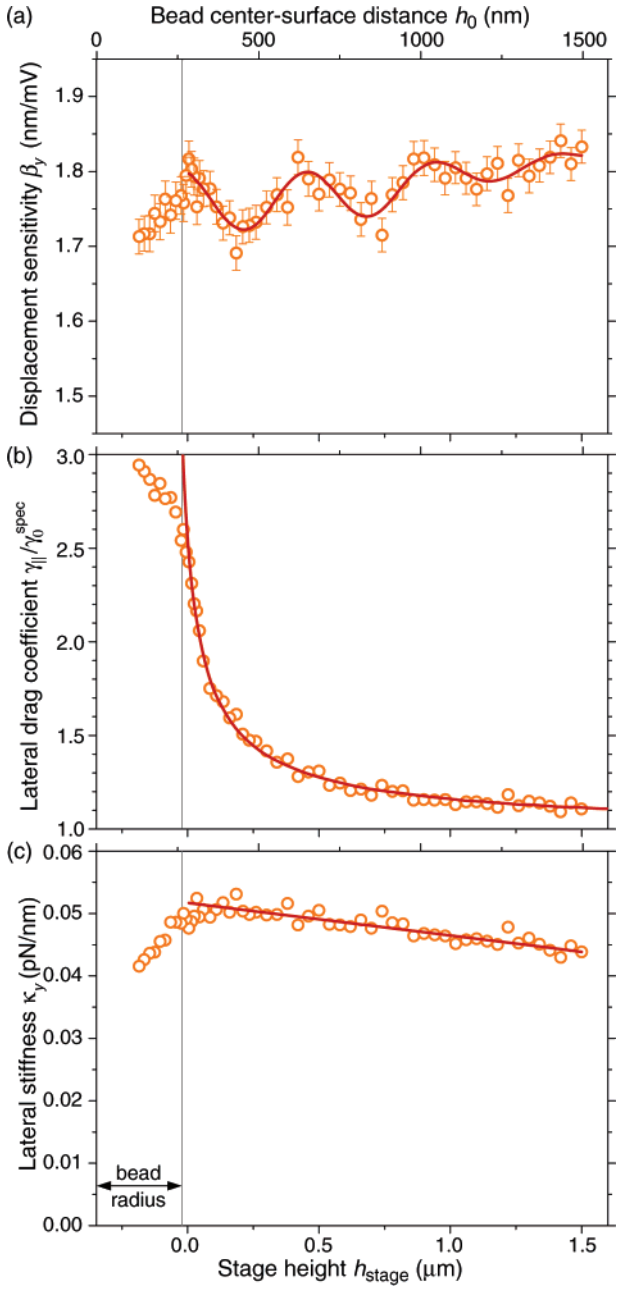

Figure 3. Displacement sensitivity (a), lateral drag coefficient (b), and trap stiffness (c) as a function of distance from a surface for a 528 nm diameter PS bead in 0.1 M KCl. The stage height has an arbitrary offset. The upper scale shows the bead center−surface separation corrected for the offset and focal shift. The vertical gray line indicates where the bead touches the surface. (a) β_y shows a modulation caused by the interference of light reflected between the bead and the surface. It is fitted by a damped sinusoid added onto a third-degree polynomial. The periodicity is 488 ± 14 nm with an amplitude of ∼2.2%, resulting in a focal shift of $\delta = 0.82 \pm 0.02$. (b) Faxén's law is fitted to $\gamma_{||}$ in units of γ_0^{spec}, resulting in an extrapolated bulk value of the drag coefficient $\gamma_0/\gamma_0^{spec} = 1.004 \pm 0.004$ and an offset of $h_{surf} = -0.347 \pm 0.002$ μm. (c) The red line is a fit to the stiffness data (circles) showing a linear decrease due to aberrations of −(12 ± 1)%/μm of bead−surface separation.

consequently restricted the fitting range to this limit. We looked for systematic deviations for $\gamma_{||}/\gamma_0 > 1.7$,[25] but did not see any within the error bars. Faxén's law was a good description of the data up to $\gamma_{||}/\gamma_0 \approx 2.4$ with normally distributed residuals of $\lesssim$4%.

The measured trap stiffness showed the expected weakening away from the surface. In Figure 3c, the lateral stiffness κ is plotted. It shows a maximal value at the surface with a linear decrease of −(12 ± 1)%/μm of bead−surface separation. The decrease is expected because of spherical aberration and is consistent with previously published values.[26,27] Figure 3 reveals that, if a calibration is performed far away from the coverslip assuming $\gamma = \gamma_0^{spec}$, aberrations can significantly reduce the measured stiffness. Thus, if this stiffness value is subsequently used close to the surface, errors in force measurements can be large.

The lateral calibration is precise and accurate. The average relative errors on β, γ, and κ obtained from data taken at a single distance to the surface were 1.5, 2.4, and 2.4%, respectively. Because γ_0 and h_{surf} result from a fit to ∼50 data points, the relative error on these parameters is reduced about 7-fold ($\sim\sqrt{50}$), resulting in a precision of ∼0.3%. The accuracy and overall error, however, is limited to ∼1% due to neglect of the frequency dependence of the drag (see section 2.3). With such a high precision, small differences in bead radius from the manufacturers specification, for instance, can be resolved[1] (see Appendix B).

The modulation seen in the displacement sensitivity due to the standing light wave is also reflected in the measured trap stiffness. Because the displacement sensitivity β is inversely proportional to the laser intensity, we expect that the modulation seen in the displacement sensitivity reflects a modulation in laser intensity and should therefore also be present in the trap stiffness which depends linearly on the laser intensity. This modulation is indeed seen when f_c is plotted as a function of height (data not shown). However, since the modulation is only 5% peak-to-peak in Figure 3a for the 0.5 μm diameter PS bead, it is comparable to the error in κ which consequently masks the effect in Figure 3c. The amplitude of the modulation of the displacement sensitivity depends on the refractive index, the size of the trapped bead, and the axis. For example, silica beads have a smaller refractive index and therefore scatter less light. On the other hand, for a 1 μm diameter PS bead, the amplitude of the lateral displacement sensitivity modulation is ∼5% and the axial one almost ∼25% (data not shown). For larger beads, the effect was even more pronounced, and we observed the modulation in both the lateral and axial trap stiffness (data not shown). In the following, in particular, regarding the surface force measurements, we preferred to use small silica beads.

3. Results and Discussion

The axial direction is calibrated by using the measured bulk drag coefficient γ_0 and surface position h_{surf} obtained from the lateral calibration together with the analysis of the power spectra of the z direction. Once calibrated, the expected dynamic axial forces arising from the hydrodynamic interaction with the surface can be deduced and confirmed in a self-consistent manner. In addition, static surface forces and surface force gradients can be measured.

3.1. Dynamic Axial Forces. As was the case for the lateral direction, three parameters have to be determined by the axial calibration: the axial drag coefficient $\gamma_\perp$, displacement sensitivity β_z, and stiffness κ_z. With the known surface position h_{surf}, eq 12 exactly defines the height h of the bead above the surface. Together with the measured bulk drag coefficient γ_0, eq 6 yields the axial drag coefficient $\gamma_\perp(\gamma_0, h)$. Once $\gamma_\perp$ is known, eq 8 solved for the axial displacement sensitivity results in

$$\beta_z = \sqrt{\frac{k_B T}{\gamma_\perp D^z_{volts}}} \tag{13}$$

and the axial stiffness is readily obtained by

(26) Florin, E. L.; Pralle, A.; Stelzer, E. H. K.; Hörber, J. K. H. *Appl. Phys. A: Mater. Sci. Process.* **1998**, *66*, S75−S78.
(27) Vermeulen, K. C.; Wuite, G. J. L.; Stienen, G. J. M.; Schmidt, C. F. *Appl. Opt.* **2006**, *45* (8), 1812−1819.

$$\kappa_z = 2\pi f_c^z \gamma_\perp \quad (14)$$

where D^z_{volts} and f^z_c are the fitted values for the axial power spectrum (see Figure 2b). Thus, driving in one lateral direction is sufficient to calibrate the axial direction as well. The other lateral direction can be analyzed in an analogous manner.

The height dependence of the measured axial parameters confirmed the expected behavior. We used a 600 nm diameter silica bead in a 0.1 M KCl solution. At this concentration, the Debye screening length is <1 nm such that the surface forces are practically zero for bead−surface separations ≳50 nm. Cleaned glass coverslips were used with no further blocking. The axial trap stiffness κ_z determined by eq 14 is shown in Figure 4b as a function of stage height (bottom scale). The distance to the surface was varied by moving the piezo stage. The axial trap stiffness shows a maximum at the surface with a linear decrease of $-(9.0 \pm 0.3)\%/\mu$m of bead−surface separation (green line). The decrease is expected because of aberrations[26,27] and has a similar magnitude as in the case of the lateral signals (Figure 3c).

Instead of assuming the height profile of the axial drag coefficient in order to calculate the trap stiffness, we can alternatively assume a linearly decreasing trap stiffness to calculate the axial drag coefficient. In principle, one can measure this decrease far away from the surface where hydrodynamic corrections are subdominant. We used the fitted line in Figure 4b as the actual axial trap stiffness $\kappa_z^{fit}(h)$. Then, eq 14 can be inverted to calculate the axial drag coefficient $\gamma_\perp = \kappa_z^{fit}(h)/(2\pi f_c^z)$. The results are plotted in Figure 4a in units of the bulk drag coefficient γ_0 (green circles). For comparison, the lateral drag coefficient (orange diamonds) with the corresponding fit to Faxén's law (red line) is shown. The axial drag increases dramatically on approaching the surface, yet is still well-described by our interpolation formula eq 6 (green line, not a fit). Residuals are normally distributed with deviations of less than 5%. Note that the data in Figure 4a are essentially the same as those in Figure 4b. They are shown in this representation to illustrate the stronger height dependence of the axial drag compared to the lateral one. In addition, it confirms in a self-consistent manner the assumptions. Hence, it is strictly speaking not a direct measurement of the axial drag coefficient. A direct measurement can, in principle, be done by exciting the stage in the axial direction, but this approach has other limitations. For the bead−surface distances and solutions used in this study, we do not expect any deviations from the height profile of the drag coefficient.

3.2. Surface Force Gradients. *3.2.1. Procedure.* With the precise axial calibration, static surface forces can be measured based on excess deviations in the trapping position and stiffness. In Figure 5, we illustrate how the gradient of the surface forces (ϕ'' in eq 11) is obtained. The example given is for a 10^{-5} M KCl solution. For this low ionic strength, we expect a large screening length L (eq 2) and therefore a pronounced, long-range interaction of the bead with the surface. We first analyzed the axial displacement sensitivity and stiffness as outlined in the previous section, that is, ignoring surface forces. This resulted in the data points marked as gray circles in Figure 5a,b. For the gray circles, the bottom axis corresponds to the bead−surface separation $h_0 - R$ where h_0 was based only on the relative stage position (eq 12).

The surface influence becomes evident for small separations. For positions ≲200 nm, the displacement sensitivity and stiffness do not follow a linear behavior. The black lines are fits to the data far away from the surface in the range of $300 \lesssim h - R \lesssim$ 1900 nm. The deviations from these lines indicated the presence of surface interactions. This makes the use of eq 12 invalid. Instead, eq 10 that accounts for the surface interactions is necessary. The displacement Δh of the bead from the center position of the optical potential caused by the surface forces was measured by an extra change in the laser intensity on the detector as a function of height, $\Delta h = \beta_z \Delta I$, where ΔI is the extra deviation of the laser intensity. This deviation is the difference between the solid blue circles (the laser intensity) and the dashed line in Figure 5a. Because the gray circles were based on the height defined in eq 12, the axial drag was overestimated. The correctly processed data are plotted with the correct bead−surface separation as red circles. For the data point closest to the surface, $\Delta h \approx 60$ nm (not all gray circles are shown for the stiffness data). For this data point, the use of eq 10 compared to eq 12 changed the effective axial stiffness by more than a factor of 2. Note that, since both the axial displacement sensitivity and the trap stiffness calculations are based on the same drag profile and only the trap stiffness shows an effect upon approaching the surface (a deviation from linear behavior), this

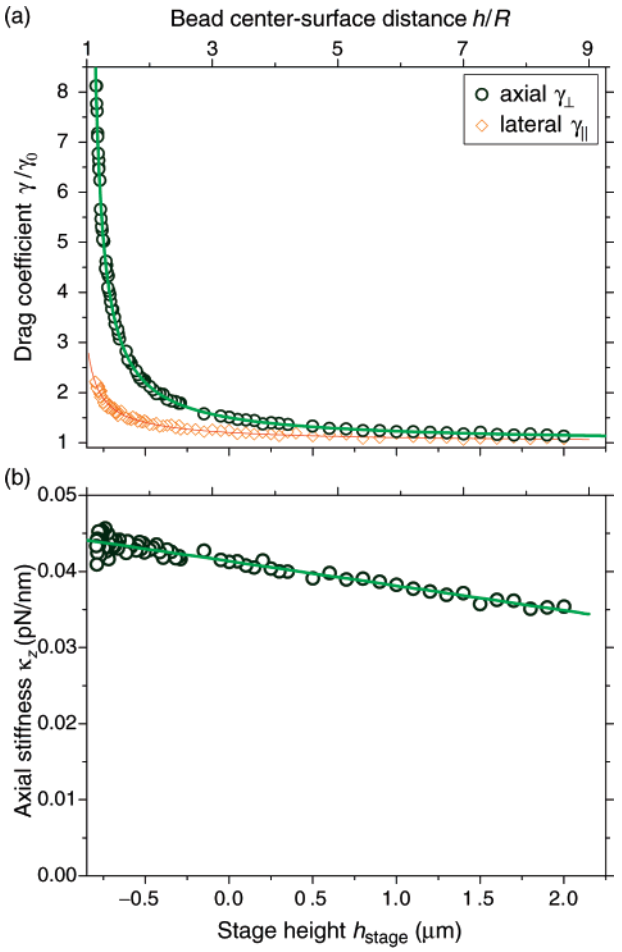

Figure 4. Axial drag (a) and axial stiffness (b) as a function of stage position for a 600 nm diameter silica bead in a 0.1 M KCl solution ($\phi' \approx 0$ for $h/R \gtrsim 1.15$). The stage height has an arbitrary offset. The upper scale shows the bead center−surface separation in units of the bead radius. (a) The axial drag coefficient (green circles) in units of γ_0 increases by more than a factor of 8 upon approaching the surface. In comparison, the lateral drag coefficient (orange diamonds) only doubles. The solid red line is a fit to Faxén's law, and the green line corresponds to a higher order interpolation formula (see text for details). (b) The axial stiffness κ_z (green circles) shows a linear decrease due to aberrations with a slope $-(9.0 \pm 0.3)\%/\mu$m of bead−surface separation. This decrease is comparable to the lateral one (see Figure 3).

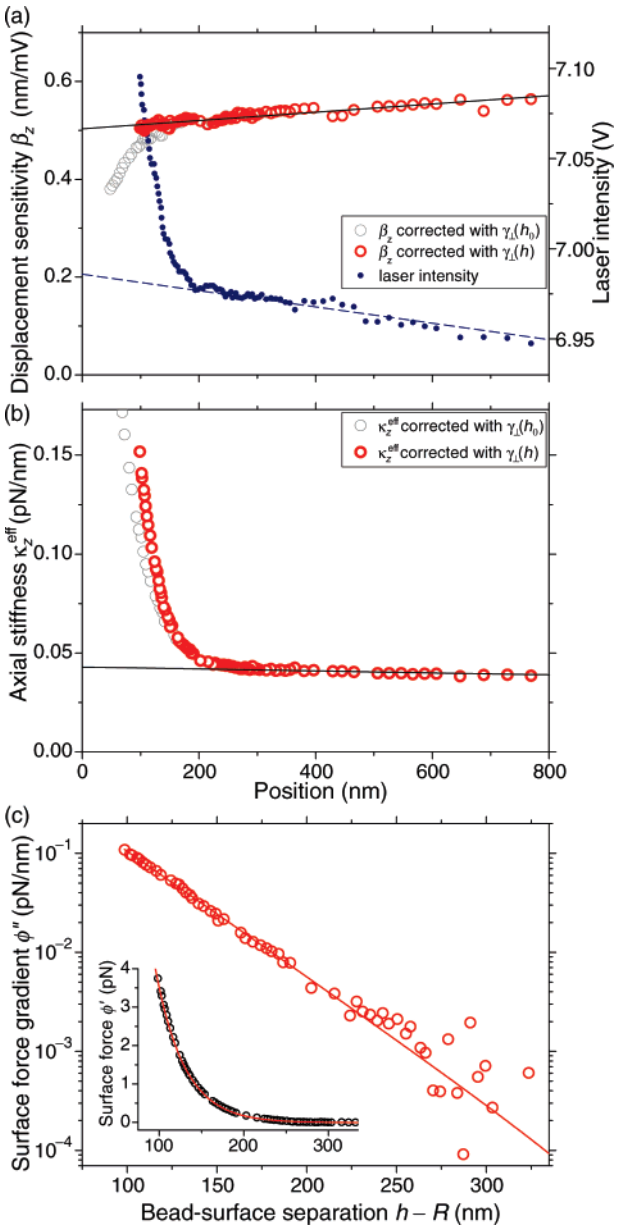

Figure 5. Illustration of how the surface force gradient is calculated for a 600 nm diameter silica bead interacting with a bare glass surface in a 10^{-5} M KCl solution (a,b). The axial displacement sensitivity (a) and stiffness (b) corrected for the height dependence of the axial drag based on the height of eq 12 (no surface effects) resulted in the gray circles. For positions $\lesssim$200 nm, the surface forces shifted the mean axial position of the bead in the trap by Δh (eq 10) which is indicated by the deviation of the laser intensity from a straight line (blue solid circles and dashed line in (a), right-hand scale). If $\gamma_\perp$ is calculated taking surface effect into account (eq 10), the red circles resulted. Finally, a linear fit to the stiffness data far away from the surface was subtracted (black line). The resulting force gradient is shown in (c) on a semilogarithmic plot. The solid line is a fit of the DLVO theory. Note that the surface position was not used as a fit parameter. The inset shows the integrated surface force gradient.

effect can be attributed solely to the static surface potential and not to a falsely assumed drag profile. If the profile would be wrong, the displacement sensitivity would also show a deviation from the expected linear behavior.

Finally, in order to determine the surface force gradient ϕ'', the contribution from the optical potential needs to be subtracted according to eq 11. This is done by subtracting the value of the black line from that of the red circles in Figure 5b. The resulting difference is the surface force gradient, plotted in Figure 5c on a semilogarithmic scale. It shows an exponential dependence on the bead−surface separation over more than 2 orders of magnitude. The solid line is a fit of the second derivative with respect to h, ϕ'', of the DLVO surface interaction potential (eq 1). The secondary potential minimum due to the attractive part of the van der Waals potential[5] is too small to be resolved for this bead.[9] As fixed parameters entering eq 1 we used $\epsilon_w = 80$ and $H = 8 \times 10^{-21}$ J. The Hamaker constant is calculated using the Lifshitz theory (glass, $\epsilon_{glass} = 2.25$ and $n_{glass} = 1.5$; silica, $\epsilon_{SiOx} = 3.8$ and $n_{SiOx} = 1.45$).[5] The exact value of H, however, was not so important since the surface interactions are dominated by the electrostatic term giving rise to the exponential behavior of the surface force gradient in Figure 5c; that is, the van der Waals interactions are negligible. Only the screening length L and the surface potential ψ_0 were used as fit parameters. Here, $L = 34.3 \pm 0.3$ nm and $\psi_0 = 29.3 \pm 0.1$ mV. We discuss these values in the next section. Note that the surface position is fixed from the fit to the lateral drag coefficient. The integrated surface force gradient (inset, Figure 5c) shows that the surface forces are in the pN range. The direct surface force measurement based on the first derivative of the interaction energy ϕ' in eq 10 yields a comparable result (data not shown). However, the mean error on the directly measured force is ~10-fold higher compared to the integrated values. The latter have an error of 10 fN based on the standard deviation of the residuals derived from the fit of the DLVO theory. This is the reason why we used the second derivative ϕ'' to measure the surface forces. From a mathematical point of view, there is no difference whether one measures the first or second derivative of ϕ based on eq 10 or eq 11, respectively. The advantage of measuring the second derivative can be motivated in the following manner (see also section 3.2.3): One can think of it as a "lock-in amplifier technique" which senses the gradient instead of the force itself. In contrast to a conventional lock-in amplifier, we use a broad range of frequencies generated by the Brownian motion. Lock-in techniques act as bandpass filters and are thus less susceptible to especially low frequency noise.

3.2.2. Variation of the Screening Length. In order to test the above procedure, we used KCl solutions of different concentrations and compared the results to the DLVO theory. The experimental conditions and data analysis were the same as in the example of the previous section. The results are summarized in Figure 6. In Figure 6a, the surface force gradient as a function of bead−surface separation is plotted for KCl concentrations of 10^{-5} to 10^{-1} M, and purified water (ddH_2O). The lines through the data are fits to the DLVO theory. With increasing salt concentrations, the repulsive electrostatic interactions are increasingly screened and the bead consequently comes closer to the surface. For a concentration of 0.1 M, the van der Waals interactions dominate over the repulsive electrostatic interactions, resulting in an overall attractive potential—the bead is adsorbed to the surface after the last data point at $h - R \approx 50$ nm (cyan hexagons). This latter data set was used as an example in Figure 4.

The measured surface interactions agreed with the DLVO theory for intermediate salt concentrations. The fit parameters from the lines in Figure 6a are displayed in Figure 6b as a function of KCl concentration. On the left-hand axis the screening length L (colored, closed symbols) and on the right-hand side the corresponding effective surface potential ψ_0 is plotted (black, open hexagons). The solid line is the Debye length based on eq 2. The average relative error on the screening length was 15%. The main source was thermal drift (see below); the average fitting

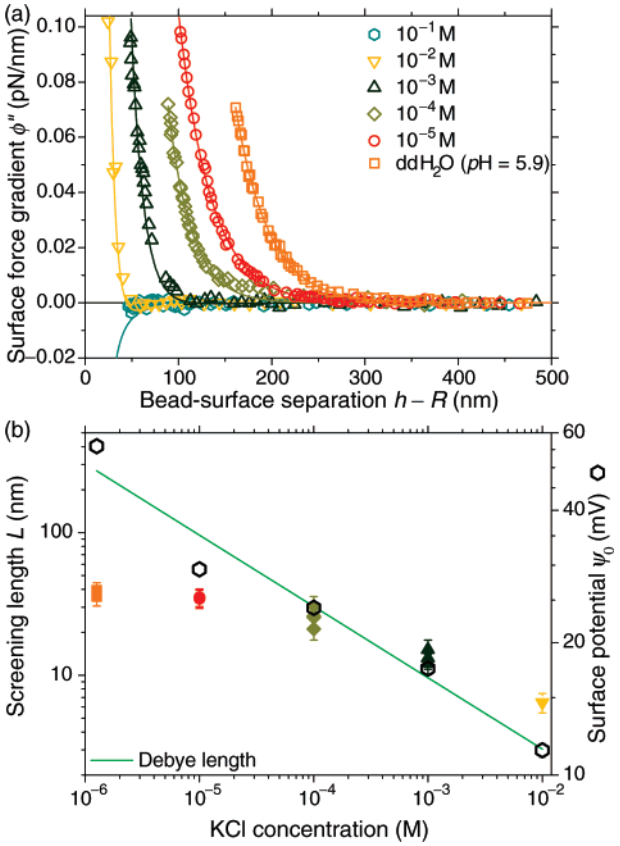

Figure 6. (a) Surface force gradients for various concentrations of KCl solutions for 600 nm diameter silica beads. The solid lines are fits of the DLVO theory using only the screening length and the surface potential as fit parameters. For the highest salt concentration (dark-cyan hexagons), the bead jumped into contact at a surface separation of ~50 nm and was thus immobilized afterward. (b) Screening length (solid symbols, left-hand axis) and surface potential (open hexagons, right-hand axis) as a function of ionic concentration obtained from the fits to the surface force gradients. The solid line shows the calculated Debye screening length.

error for an individual data set was only 3%. The relative error on ψ_0 was 2%. The data show an exponential dependence on the bead−surface separation for all concentrations. However, quantitative agreement with the DLVO theory is only observed for intermediate salt concentrations. For low amounts of added salt, the screening length is too small compared to the Debye length, and for high concentrations, it is too large. For low concentrations and the purified water, deviations are likely caused by multivalent ionic contaminations and the slightly acidic pH. The water had a pH of 5.9, probably due to the CO_2 from the atmosphere. Our measured L values for these conditions are comparable to the ones measured by Hansen et al.[9] For the high concentration, we do not know the cause of the discrepancy. The effective surface potential ψ_0 shows a scaling of $[KCl]^{-1/2}$. Its magnitude is in the lower range of previously published values.[6] The low values are indicative of an acidic pH and that some of the surface charges are exchange ions.[5,6] The effective surface potential ψ_0 was error-prone in previous tweezers studies[8,9] due to the larger uncertainty in the surface position and was therefore either not specified or taken as constant.

3.2.3. Restrictions. There are certain limits to the described method. Close to the surface, the trapping potential is skewed, and the drag depends on h. It was shown[8] that using a Lorentzian fit for the power spectra is a valid approach if the potential is only slightly skewed and the drag coefficient can be locally approximated by a linear dependence on the distance. These

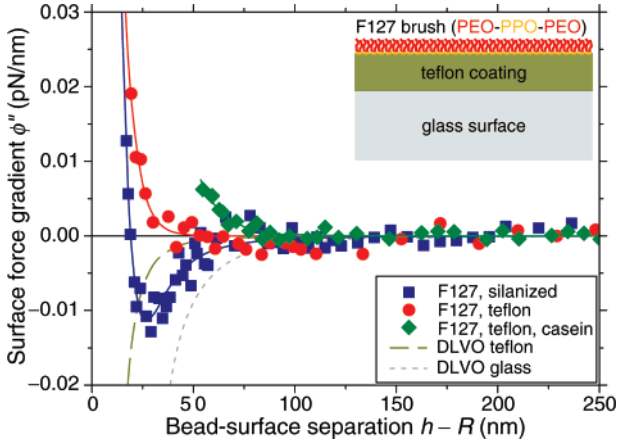

Figure 7. Surface force gradient for F127-treated, silanized (blue squares), and Teflon-coated surfaces (inset) in the presence (green diamonds) and absence of casein (red circles). Electrostatic effects are largely screened for all samples. The buffer BRB80 has about the same ionic strength as a 0.16 M KCl solution. Solid lines are fits of a DLVO-type expression to the data to guide the eye. For a bare glass (gray dotted) and Teflon (brown dashed) surface without F127 and 0.1 M KCl concentration, the purely attractive DLVO theory predictions are shown. We used $L = 1$ nm and $\psi_0 = 10$ mV, yielding $H_{glass} = 1.4 \times 10^{-20}$ J and $H_{teflon} = 1.3 \times 10^{-21}$ J (note that H is larger for PS than for silica beads, compare with section 3.2.1; PS: $\epsilon_{PS} = 2.5$ and $n_{PS} = 1.59$; Teflon: $\epsilon_{teflon} = 1.93$ and $n_{teflon} = 1.31$).

requirements are best met by a stiff trap. We used $\kappa_z \approx 0.015-0.075$ pN/nm. We did not detect any systematic deviations from a Lorentzian for the data presented. Furthermore, we excluded data points for which the bead−surface distance was smaller than 2.5 standard deviations of the Brownian motion in the z direction. This roughly corresponds to the distance where the power spectrum is affected because of the bead's motion becoming restricted by the surface. For smaller distances, the χ^2 value of the fit to the power spectrum increased significantly. The standing light wave did not limit the measurements.[8] Since we measured the modulation due to the interference effect of the displacement sensitivity and the laser intensity, we could account for the effect.

The value of the surface position is the most critical parameter in determining the surface force gradient especially for small bead−surface separations. For improved accuracy in determining h_{surf}, the height dependence of the corner frequencies can be fitted in addition to the lateral drag. For the data in Figure 7, we used the surface position as a global fit parameter for the height dependence of the three axes' corner frequencies plus that of the lateral drag coefficient. As an internal control for the correction, we confirmed that the axial displacement sensitivity did not deviate from the expected behavior (see Figure 5).

Figure 5a shows why it is important to have a stable laser intensity. In the case of back-focal-plane detection, the z position is proportional to modulations in laser intensity caused by the axial movement of the bead. Since a large offset in laser intensity needs to be subtracted (here ~7 V) a small, low-frequency intensity fluctuation of the laser itself cannot be distinguished from a true movement. For instance, a 0.5% variation corresponds to $\Delta h \approx 18$ nm ($\beta_z \approx 0.5$ nm/mV) and an error in force of almost 1 pN. This is why the direct surface force measurement based on ϕ' has a larger error than the surface force calculated by integrating the measured ϕ''; ϕ'' does not directly depend on Δh and hence is insensitive to errors on this parameter (see also section 3.2.1).

We checked for effects of thermal drift during the calibration process because this directly affects the screening length. If we

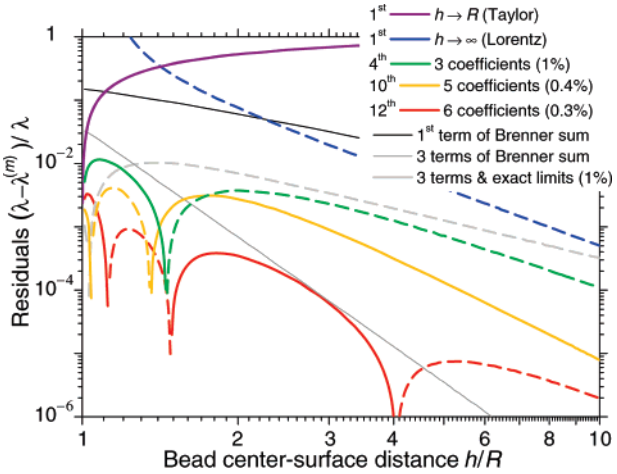

Figure 8. Goodness of interpolation formulas compared to Brenner's exact result (see also Table 1). Normalized deviations of the *m*th-order interpolation equations from the λ values based on Brenner's infinite series (eq 17) as a function of distance from the surface in units of the bead radius on a double logarithmic plot. Negative residuals are plotted with dashed lines. The parameters for the equations are given in Table 1. The 12th-order equation (eq 6) deviates less than $\lesssim$0.3% for all distances.

repeat the calibration for the same bead and determine the surface position h_{surf} again, the difference to the previous value gives a measure for the drift. We kept the temperature as constant as possible during the measurements and worked in a thermally well equilibrated room. The acquisition of the data and the automatic fitting of the power spectra with either 4096 or 8196 data points at a single height position took ~7 or ~15 s, respectively. With typically ~80 positions, the complete calibration as a function of distance took about 10 or 20 min. During this time, there was a drift of ~1−2 nm/min depending on the sample. This drift is included in the error bars in Figure 6b and thus cannot account for the deviations from the DLVO theory. With temperature monitoring and the capability of exactly measuring the surface position, we can, in principle, correct for all effects that are due to thermal drift. This is an advantage of the method presented here.

3.2.4. Blocked Surfaces and Casein. We applied our method to measure the surface interaction of microspheres with surfaces that are coated in such a way as to prevent the beads from sticking to them. Under physiological relevant conditions, the repulsive electrostatic interactions are largely screened, and the attractive van der Waals forces dominate the interaction of colloids near surfaces unless they are treated further. The data for these blocked surfaces are shown in Figure 7. For these measurements, we used the 528 nm diameter PS beads in either a 0.1 M KCl solution or a 0.2 mg/mL casein solution in BRB80 (80 mM PIPES/KOH, pH 6.9, 1 mM $MgCl_2$, 1 mM EGTA). For both solutions, the Debye length is $\lesssim$1 nm. For individual power spectra, only 4096 data points were used to shorten the data acquisition time.

We used the blocking agent F127 to pacify the surfaces. The hydrophobic middle block of the F127 (section 2.2) requires a hydrophobic surface for stable adsorption.[17] We used two different methods to render surfaces hydrophobic. We coated glass surfaces with either a self-assembled monolayer of dichlorodimethylsilane (DDMS) or a Teflon layer (see section 2.2). The difference between the two methods is the thickness and refractive index of the coated film. While the thin ($\lesssim$2 nm) DDMS layer only slightly affects the Hamaker constant and thus the van der Waals interactions between the bead and the surface,[5] the comparatively thick ($\lesssim$100 nm) Teflon layer reduces the

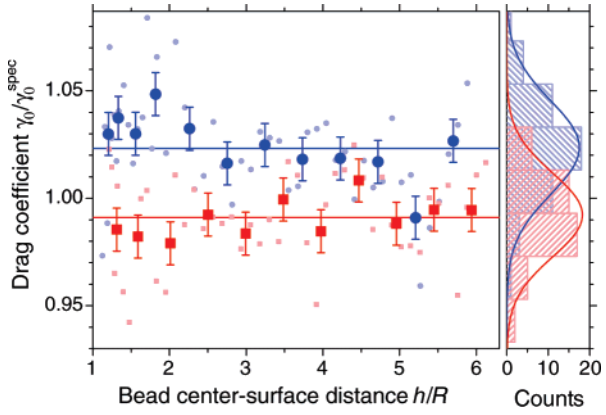

Figure 9. Bead individuality. Once the distance to the surface is known, the height dependence of the drag coefficient can be removed using Faxén's law. In this way, an estimate for the bulk drag coefficient is obtained at every height. Data are shown for two different beads (blue circles and red squares). The small data points are the raw data, and the large data points are four neighboring small points binned with corresponding standard deviations shown as error bars. On the right-hand side, a histogram of the drag with a bin width of 2% is plotted. A Gaussian fit returned 1.024 ± 0.003 (N = 49) and 0.992 ± 0.003 (N = 45) (mean ± standard error of the mean). Since the standard error is much smaller than the difference between the means, differences in the bulk drag coefficient are attributed to different bead sizes.

Hamaker constant more than 10-fold compared to a bare glass surface. The reason for this reduction is that the Teflon index-matches water.[5] The inset in Figure 7 shows schematically the Teflon surface treatment.

The measured surface force gradients confirm the expected screening behavior of the Teflon surface (Figure 7). The DDMS-coated surface (silanized) shows a clear attractive region close to the surface due to the attractive van der Waals interactions (blue squares). The solid line through the data is a fit of a DLVO-type expression to guide the eye. In contrast, the Teflon-coated surface shows a purely repulsive surface force gradient (red circles) converging for small separations with the DDMS data. Due to the much smaller Hamaker constant, no attractive potential is visible within the given resolution. The strength of the attractive part for the DDMS data lies in between what is expected for the DLVO behavior for an uncoated, bare glass surface (dotted gray line) and a Teflon-coated surface without F127 (brown dashed line). The reason for this is likely because both the DDMS and more so the F127 layer lower the effective van der Waals interactions. Uncertainties in h_{surf} and the laser intensity may also contribute. On the basis of the integrated force gradient, the maximal attractive force acting on the bead is about −0.2 pN and the potential has a depth of ~1k_BT.

With the Teflon-coated surface blocked with F127 and casein in solution, we observed a long-ranged repulsive potential (green diamonds). With casein on a bare glass surface, we expect in addition to the repulsive part a short-ranged attractive region analogous to the DDMS case. Beads coated with casein and the molecular motor kinesin walking on a microtubule that is immobilized via antibodies on a surface[2] are often used to probe the mechanics of the motor. Our casein data suggest that bead motility assays might be affected by surface forces. Depending on the surface treatment in these assays, the bead might either be pushed up by the surface forces and exert an axial force on the motor protein or could be pulled down next to the microtubule leading to an asymmetry in the gate of the motor. In Figure 7, for the casein data at a distance of ~50 nm, the force is repulsive and ~0.1 pN based on the integrated surface force gradient. It

Table 1. Interpolation Coefficients of Equation 19 for *m*th Order Using *N* Coefficients

m	*N*	c_1	c_3	c_4	c_5	c_8	c_{10}	c_{11}	c_{12}	$h \to R$[a]	$h \to \infty$[a]	accuracy	comment
	1									×		10%, $h/R \lesssim 1.07$	Taylor,[28] eq 18
1	1	−9/8									×	1%, $h/R \gtrsim 4$	Lorentz[29]
3	2	−9/8	1/2								×	1%, $h/R \gtrsim 3$	Wakiya,[30] eq 16
4	3	−9/8	3/8	−1/4						×	×	1%	
10	5	−9/8	1/2	−37/80		1/5	−9/80			×	×	0.4%	
12	6	−9/8	1/2	−57/100	1/5			7/200	−1/25	×	×	0.3%	eq 6

[a] Whether the corresponding behavior of the limits of h going to R and ∞ is satisfied exactly is indicated by a "×".

is more than 6-fold the lateral drag force that the bead experiences if it were pulled by a kinesin with a speed of 800 nm/s. This means that the bead is not trailing behind the kinesin motor but is rather centered above it. In addition to these geometric effects, the mechanochemistry might be affected.[2]

4. Conclusion

We have described two new methods in this paper. First, the calibration method in Tolić-Nørrelykke et al.[1] has been extended to calibrate optical tweezers in all spatial dimensions as a function of distance from a surface. With this technique, no assumptions have to be made about the system and all parameters affecting the trapping conditions are measured. Importantly, interference effects that modulate the laser intensity away from the surface are accounted for in this way. Furthermore, aberrations arising from oil-immersion objectives or improperly adjusted water immersion objectives can be evaluated. Thus, it is not necessary to work with expensive water immersion objectives only for the reason of avoiding aberrations. Second, we applied the calibration technique to measure surface interaction potentials with microspheres of a diameter of <1 μm. These are smaller than microspheres utilized in earlier studies[7−9] and of a size often used in biophysical single-molecule experiments. It is feasible to measure surface interactions for even smaller beads. The technique is sensitive enough to detect surface force gradients of ∼1 fN/nm. We tested the method against the DLVO theory and found quantitative agreement for 10^{-5} M $\lesssim$ [KCl] $\lesssim 10^{-2}$ M. Furthermore, the method was applied in more complex systems relevant to biological experiments.

Appendix A. Closed-Form Interpolation Formulas for the Axial (Wall) Drag

The height dependence of the drag coefficient is stronger upon approaching a wall for the axial drag compared to the lateral one. While the increase of the lateral drag is well described by Faxén's law, an analogous closed-form equation is lacking for the axial dimension. In this appendix, we use the exact creeping flow solution from Brenner,[11] an infinite series, to derive simple equations that approximate the distance dependence of the axial drag coefficient to within 1% or less. We restrict the discussion to the zero-frequency limit of the drag coefficient.

A sphere moving toward or away from a solid surface experiences a resistance or *wall drag*

$$F_z = \gamma_0 \lambda v_z = \gamma_\perp v_z \tag{15}$$

with the velocity in the axial direction v_z, the Stokes drag coefficient γ_0, and the axial drag coefficient $\gamma_\perp$; $\lambda = \lambda(R/h)$ is a correction to Stokes' law.

For $h/R \gg 1$, Lorentz[29] derived an equation up to first order in R/h. On the basis of the method of reflections, Wakiya[30] calculated a correction up to third order

$$\lambda^{(3)} = \frac{1}{1 - \frac{9}{8}\left(\frac{R}{h}\right) + \frac{1}{2}\left(\frac{R}{h}\right)^3} \tag{16}$$

In the limit of a creeping flow approximation, Brenner[4,11] solved the problem exactly

$$\lambda = \frac{4}{3}\sinh\alpha \sum_{n=1}^{\infty} \frac{n(n+1)}{(2n-1)(2n+3)} \times \left[\frac{4\cosh^2\left(n+\frac{1}{2}\right)\alpha + (2n+1)^2\sinh^2\alpha}{2\sinh(2n+1)\alpha - (2n+1)\sinh 2\alpha} - 1\right] \tag{17}$$

with $\alpha = \cosh^{-1}(h/R)$. For $h \to \infty$, $\lambda = 1$, which makes the axial drag coefficient correspond to the Stokes' bulk drag coefficient. In the other limit of $h \to R$, λ in eq 17 diverges ($\lambda \to \infty$). The limit of small separations, $h \approx R$, is attributed to G. I. Taylor[28]

$$\lambda^{(h\to R)} = \frac{R}{h-R} \tag{18}$$

Sedimentation experiments[31] in silicone oil with nylon spheres with a radius of around 2 mm confirmed eq 17 and eq 18 down to a sphere−surface separation of ∼0.11R. At this distance, the axial drag coefficient is more than 10 times the Stokes drag.

While eq 17 is exact, it cannot be used for fitting data as it stands because of its infinitely many terms. One can either truncate the sum at $n = n_{max}$ or use rational polynomial functions in order to approximate eq 17. In case of the truncation and large distances, the sum converges rapidly, and $n_{max} = 2$ is sufficient for a $\lesssim$1% deviation from eq 17 for $h/R > 1.8$. For small separations, the convergence is rather slow since every term has a singularity at $h = R$. For a 1% accuracy down to $h/R = 1.1$, n should be at least 4. Achieving this accuracy down to 1% of the radius ($h/R = 1.01$) requires $n_{max} \geq 6$. For a 0.1% accuracy, $n_{max} \geq 15$.

In the spirit of Padé approximants, the dependence of the axial drag on h/R can be approximated by a mth-order equation of the form

$$\lambda^{(m)} = \frac{1}{1 + c_1\left(\frac{R}{h}\right) + c_2\left(\frac{R}{h}\right)^2 + \ldots + c_m\left(\frac{R}{h}\right)^m} \tag{19}$$

We can determine the coefficients c_m numerically for a certain range of h by fitting this equation to numerical values of the axial

(28) Hardy, W.; Bircumshaw, I. *Proc. R. Soc. London, Ser. A* **1925**, *108* (745), 1−27.
(29) Lorentz, H. *Abhandl. Theoret. Phys.* **1906**, *1*, 23.
(30) Wakiya, S. *Res. Rep. Fac. Eng. Niigata Univ. (Japan)* **1960**, *9*, 31.
(31) MacKay, G.; Suzuki, M.; Mason, S. *J. Colloid Sci.* **1963**, *18*, 103−104.

drag coefficient calculated from Brenner's infinite series (eq 17). Analytically, the limiting case of eq 18 puts two constraints on the parameters c_m if eq 19 is supposed to hold for $h \rightarrow R$

$$\sum_{k=1}^{m} c_k = -1 \text{ and } \sum_{k=1}^{m} k c_k = -1 \qquad (20)$$

One can either use the constraints in the fitting procedure such that both limits are fulfilled or relax the constraints to achieve a better fit in a certain region of interest.

There are many sets of parameters that fulfill the above requirements. The simplest is derived in the following manner. The limit for $h \rightarrow \infty$ implies that $c_1 = -9/8$. Together with the two constraints from eq 20, at least a third-order equation is required. Using $c_2 = 0$ from eq 16 results in a 4th-order equation with $c_3 = 3/8$ and $c_4 = -1/4$. This equation deviates less than ~1% over the whole range of h. If one does not require $c_2 = 0$, a third-order equation can be derived. This equation, however, deviates up to 4% with the same number of coefficients.

In order to develop a better approximation, we used a numerical procedure. With the program Mathematica (Wolfram Research, Inc.), we evaluated eq 17 numerically. Subsequently, we fitted eq 19 to the calculated λ values. We calculated 900 values for λ in the range of $1.01 \leq h/R \leq 10$ with 0.01 increments for h/R. The upper limit in the sum of eq 17 was $n = 100$. Increasing n to 1000 only changed the 13th significant digit of the value calculated at $h/R = 1.01$.

We fitted the data by a Levenberg−Marquart algorithm, either constraining the coefficients of eq 19 to satisfy eq 20 or not (all parameters free). As weights we used the values of eq 17. On constraining the parameters, it turned out that it was necessary to use high order coefficients to obtain a good approximation for $h/R \approx 1$. A 10th-order equation with five coefficients (the others set to zero) deviates less than 0.4% over the whole range. The maximum deviation occurs at $h/R \approx 1.14$. Increasing the number of coefficients and going to higher order improves the approximation only slightly. A 12th-order equation with six coefficients deviates less than 0.3% over the whole range (eq 6). Here, the maximum deviation occurs at $h/R \approx 1.02$. This approximation is better than 0.1% for $h/R \gtrsim 1.1$. Going either to even higher order or increasing the number of coefficients further did not improve the approximation significantly.

Figure 8 and Table 1 summarize the results. The residuals, the normalized deviation from Brenner's sum (eq 17), are illustrated in Figure 8, and the corresponding coefficients for the equations are given in Table 1. The first-order equation for large separations (Lorentz) agrees to within 1% with eq 17 only for $h/R \gtrsim 4$. In the other limit, eq 18 deviates by 10% for $h/R \lesssim 1.07$. Using the first three terms of eq 17 ($n_{max} = 3$) plus a correction $43R^2/[1323h(h-R)]$ to compensate the lacking terms at the singularity $h = R$ only achieves an approximation comparable to the fourth-order equation which uses only three coefficients. In a Padé approximation, the numerator often is a higher order polynomial as well. When using such a polynomial, more constraints analogous to eq 20 are invoked which require in total at least six coefficients. The simplest version with a third-order polynomial in both the numerator and denominator only achieves an accuracy of 0.8% over the whole range of h. Along those lines, Bevan et al.[32] developed a similar formula which deviates by 0.7% using five coefficients which, however, does not follow the first-order scaling of Lorentz ($c_1 \neq -9/8$).

Appendix B. Bead Individuality

The calibration method described in section 2.6 and Tolić-Nørrelykke et al.[1] is able to resolve small differences in bead radius. Two beads (3 and 17 from Tolić-Nørrelykke et al.[1]) were analyzed in the same manner as the one in Figure 3b (bead 12 in Tolić-Nørrelykke et al.[1]). After fitting the data to Faxén's law (eq 5), the height dependence was removed by dividing the measured drag coefficient with $\gamma_{||}(h)/\gamma_{0.}$ The data is then plotted in units of γ_0^{spec} (Figure 9). The mean value of the measured bulk drag coefficient γ_0 for the two beads differs by more than 3% with a standard error of the mean of only 0.3% for each bead. Since the beads were in the same flow cell and temperature variations were excluded,[1] the difference can only be explained by different bead radii (compare with Tolić-Nørrelykke et al.[1] where we analyzed a total of 24 beads but showed only the mean value for γ_0 for each bead). The deviations lie within the estimated uncertainty in γ_0^{spec} of 2.3% which is based on the polydispersity in radius specified by the manufacturer and the error in temperature determination. If experiments are performed with beads having a large polydispersity, the calibration error can be large if γ_0 is not measured directly[8,9] but assumed to be γ_0^{spec}.

Acknowledgment. We thank H. Flyvbjerg, S. Grill, V. Bormuth, and C. Dinu for critical reading of the manuscript, and H. Wolf was valuable in the machine shop.

LA0622368

(32) Bevan, M. A.; Prieve, D. C. *J. Chem. Phys.* **2000**, *113* (3), 1228−1236.